
Article:
May, S., Vignollet, J. and De Borst, R. (2015) A numerical assessment of phase-field models for brittle and cohesive fracture: Γ-Convergence and stress oscillations. European Journal of Mechanics, A/Solids, 52. pp. 72-84. ISSN: 0997-7538

https://doi.org/10.1016/j.euromechsol.2015.02.002

Accepted Manuscript

A numerical assessment of phase-field models for brittle and cohesive fracture: Γ-convergence and stress oscillations

Stefan May, Julien Vignollet, René de Borst

PII: S0997-7538(15)00015-7

DOI: 10.1016/j.euromechsol.2015.02.002

Reference: EJMSOL 3163

To appear in: *European Journal of Mechanics / A Solids*

Received Date: 11 August 2014

Revised Date: 9 February 2015

Accepted Date: 9 February 2015

Please cite this article as: May, S., Vignollet, J., de Borst, R., A numerical assessment of phase-field models for brittle and cohesive fracture: Γ-convergence and stress oscillations, *European Journal of Mechanics / A Solids* (2015), doi: 10.1016/j.euromechsol.2015.02.002.

- A numerical demonstration that in phase-field models for brittle fracture the smeared crack length does not necessarily converge to the discrete crack length upon mesh refinement.
- A demonstration that the numerical results of boundary value problems that use the phase-field model for brittle fracture are very sensitive to how the boundary conditions are applied.
- A proof that the phase-field model for cohesive fracture does not satisfy a two-dimensional patch test, even when the interpolation orders of the displacement field, the phase field and the crack-opening field are balanced.

A numerical assessment of phase-field models for brittle and cohesive fracture: Γ-convergence and stress oscillations

Stefan May[a], Julien Vignollet[a], René de Borst[a,*]

[a] *University of Glasgow, School of Engineering, Rankine Building, Oakfield Avenue, Glasgow G12 8LT, UK.*

Abstract

Recently, phase-field approaches have gained popularity as a versatile tool for simulating fracture in a smeared manner. In this paper we give a numerical assessment of two types of phase-field models. For the case of brittle fracture we focus on the question whether the functional that describes the smeared crack surface approaches the functional for the discrete crack in the limiting case that the internal length scale parameter vanishes. By a one-dimensional example we will show that Γ-convergence is not necessarily attained numerically. Next, we turn attention to cohesive fracture. The necessity to have the crack opening explicitly available as input for the cohesive traction-relative displacement relation requires the independent interpolation of this quantity. The resulting three-field problem can be solved accurately on structured meshes when using a balanced interpolation of the field variables: displacements, phase field, and crack opening. A simple patch test shows that this observation does not necessarily extend to unstructured meshes.

Keywords: phase-field model, brittle fracture, cohesive fracture, Γ-convergence, stress oscillations

1. Introduction

Ever since the first application of the finite element method to fracture there has been a debate between two competing schools. In the discrete approaches the physical phenomenon of separation is mimicked and a geometric discontinuity is created. Originally, this approach restricted crack propagation to occur along element boundaries, i.e. between elements (Ngo and Scordelis, 1967). With the advent of automatic mesh generators, remeshing has alleviated the restriction that cracks could only propagate along the element boundaries of the *initial* discretisation (Wawrzynek and Ingraffea, 1987; Camacho and Ortiz, 1996). The extended finite element method has, in principle, fully decoupled the crack propagation path from the underlying mesh lay-out, see (Belytschko and Black, 1999; Moës et al., 1999), who applied the method to brittle fracture, and Wells and Sluys (2001); Moës and Belytschko (2002); Remmers et al.

*Rene.DeBorst@glasgow.ac.uk

(2003), who used a cohesive fracture model. More recently, the fact that knot insertion lowers the order of continuity in isogeometric finite element analysis has provided a novel way to introduce cracks in solids and structures (Verhoosel et al., 2011; Hosseini et al., 2014).

Although discrete crack approaches provide a physically appealing way to introduce fracture in finite element models, the complications that ensue when describing phenomena like crack branching, coalescence, and curved crack boundaries in three dimensions tend to favour the use of smeared crack approaches. Early smeared crack approaches consist of simply modifying the linear-elastic stress-strain relation at integration point level into orthotropic elasticity (Rashid, 1968). Subsequent improvements include the replacement of a sudden stress drop to zero by a gradual softening relation (Bažant and Oh, 1983), and the use of damage mechanics as a framework to describe smeared cracking. A major step forward was the removal of the ill-posedness of the boundary value problem that is caused by smearing out the decohesion over a finite domain. Regularisation can be obtained by means of non-local approaches (Pijaudier-Cabot and Bažant, 1987), and more effectively in a finite element context, by gradient approaches (Peerlings et al., 1996), see also de Borst et al. (2004) and Pham and Marigo (2013).

Closely related to gradient damage models are the phase-field models which have become en vogue recently. Motivated by the work of Ambrosio and Tortorelli (1990), who approximated the Mumford-Shah potential (Mumford and Shah, 1989) by elliptic functionals, Francfort and Marigo (1998) have developed the variational approach to brittle fracture, which minimises the energy of the bulk and the energy of the surface associated to the crack. Based on this, Bourdin et al. (2000) developed a numerical solution strategy, in which an auxiliary field – the phase field, in which a control variable d ranges from zero to one – was introduced, which distributes the fracture energy over the volume of the solid.

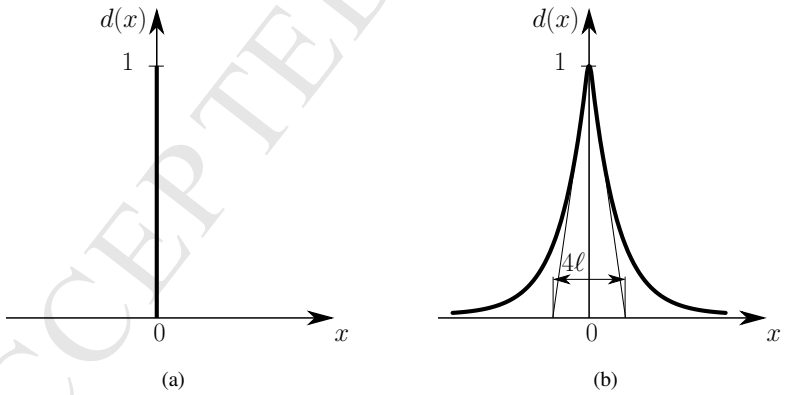

Figure 1: (a) sharp crack, and (b) smeared crack modelled with the length scale parameter ℓ

An important issue in the phase-field approach to brittle fracture is whether the functional Π_ℓ that describes the distributed or smeared crack surface, approaches the

functional Π for the discrete crack in the limiting case $\ell \to 0$, with ℓ the length scale parameter that governs the width over which the crack is distributed, Fig. 1. Note that $\Pi_\ell \to \Pi$ for $\ell \to 0$ implies that the smeared crack length Γ_ℓ converges to the discrete crack length Γ. Chambolle (2004) has proven that for continuous media this is the case, so that the functional Π_ℓ for the smeared crack surface Γ-converges to that for the discrete crack surface for a vanishing length scale parameter, that is $\ell \to 0$. Bellettini (1994) considered the Γ-convergence of the discretised version $\Pi_{\ell,h}$ of Π_ℓ and showed that $\Pi_{\ell,h}$ Γ-converges to Π for $\ell \to 0$ under the condition that $h \ll \ell$, h denoting the mesh spacing. However, this has been done in the context of image segmentation and few, if any, *numerical* investigations have been published that address the question whether Γ-convergence can be demonstrated in actual boundary value problems for the phase field model for brittle fracture. The present investigations suggest that there is a discrepancy between the theoretical and the numerical results with respect to the Γ-convergence of $\Pi_{\ell,h}$ to Π.

When extending the phase-field approach to cohesive fracture, a second auxiliary field must be introduced that captures the displacement jump (Verhoosel and de Borst, 2013). A three-field problem ensues which entails some complications with respect to the interpolation of the constituent fields. In a one-dimensional study it was found that in order to avoid stress oscillations the linear interpolations for the phase field and the smeared displacement jump had to be complemented by a cubic interpolation of the displacements in order to avoid stress oscillations. In Vignollet et al. (2014) this issue was pursued further and also for a balanced order of interpolations stress oscillations were found for two-dimensional, unstructured meshes. Herein, the issue will be addressed rigorously by numerically investigating a two-dimensional patch test.

In the next section the phase-field approach will be recapitulated briefly. This is followed by a concise description of the phase-field model for brittle fracture, a numerical assessment of Γ-convergence for a one-dimensional boundary value problem, and an investigation of the sensitivity of phase-field models to the precise imposition of boundary conditions in a two-dimensional boundary value problem. Then, the cohesive phase-field model will be summarised and be used in a two-dimensional patch test. Concluding remarks finalise the paper.

2. Phase field representation of a crack

The basic idea of phase-field models is to approximate a discontinuity Γ by a smeared surface Γ_ℓ. In a one-dimensional setting the exponential function

$$d(x) = e^{-\frac{|x|}{2\ell}} \tag{1}$$

is used to approximate the discontinuous function of Fig. 1(a). As noted before, ℓ is the internal length scale parameter. The phase-field variable $d \in [0, 1]$ describes the phase field. Herein, d is defined such that $d = 0$ characterises the intact state of the material, while $d = 1$ represents the fully broken material, similar to the definition commonly adopted in damage mechanics. For the one-dimensional case, Eq. (1) is the solution to the differential equation

$$d - 4\ell^2 d_{,xx} = 0, \tag{2}$$

where a comma denotes differentiation, and which is subject to the boundary conditions:

$$d(0) = 1, \tag{3}$$

$$d(\pm\infty) = 0. \tag{4}$$

This can be demonstrated simply by applying the Ansatz function $d = e^{-|\lambda||x|}$, which satisfies the boundary condition of Eq. (4), to Eq. (2), solving for λ and subsequently using Eq. (3) to determine the constant parameter.

Using Eq. (2) the functional Γ can be approximated by the functional Γ_ℓ

$$\Gamma_\ell = \int_\Omega \underbrace{\frac{1}{4\ell}\left(d^2 + 4\ell^2 d_{,x}{}^2\right)}_{\gamma_\ell} \mathrm{dV}, \tag{5}$$

with γ_ℓ the crack surface density function, see Miehe et al. (2010b) for details. For the one-dimensional case the approximation is exact, so that

$$\Gamma = \int_\Gamma \mathrm{dA} = \Gamma_\ell. \tag{6}$$

In a multi-dimensional setting γ_ℓ can be expanded as follows:

$$\gamma_\ell = \frac{1}{4\ell}\left(d^2 + 4\ell^2 d_{,i} d_{,i}\right). \tag{7}$$

While the discontinuity has been distributed over the entire domain Ω, as can be observed from Eq. (5), the rapid decay of the exponential function in Eq. (2) would enable that a cut-off can be applied at a finite distance of the centre of the smeared discontinuity.

3. Phase field model for brittle fracture

Bourdin et al. (2000) have proposed to model fracture using expression Eq. (1) for the phase field d. With minor modifications this approach has been adopted by, e.g., Amor et al. (2009); Kuhn and Müller (2010); Miehe et al. (2010b); Borden et al. (2012). More recently, a fourth-order phase-field model has been put forward by Borden et al. (2014), exploiting the higher-order continuity of spline functions. In Vignollet et al. (2014) concerns have been expressed that the correct crack length is not necessarily retrieved for a vanishing length scale parameter ℓ by numerically considering the example of a one-dimensional bar in tension. Herein, the study of this bar with respect to this Γ-convergence is checked numerically.

3.1. Continuum formulation of the phase-field model for brittle fracture

In the following, a brief outline of the model by Bourdin et al. (2000) is given. The potential for a solid with a discrete crack reads:

$$\Pi = \int_\Omega \psi^{\mathrm{el}} \,\mathrm{dV} + \int_\Gamma \mathcal{G}_c \,\mathrm{dA}, \tag{8}$$

where the first term denotes the elastic energy in the bulk and the second term represents the fracture energy which is created upon crack propagation. The elastic energy density ψ^{el} can be expressed by Hooke's law:

$$\psi^{\mathrm{el}} = \frac{1}{2}\lambda\varepsilon_{ii}\varepsilon_{jj} + \mu\varepsilon_{ij}\varepsilon_{ij} \tag{9}$$

as a function of the infinitesimal strain tensor

$$\varepsilon_{ij} = \frac{1}{2}\left(u_{i,j} + u_{j,i}\right) \tag{10}$$

with λ and μ the Lamé constants, while u_i denotes the displacement. In Eq. (8), $\mathcal{G}_c$ is the fracture energy, i.e. the amount of energy needed to create a unit area of fracture surface. Using Eq. (5) the fracture energy necessary to create a diffusive crack can be expressed as:

$$\int_\Gamma \mathcal{G}_c \,\mathrm{dA} = \int_\Omega \mathcal{G}_c \gamma_\ell \,\mathrm{dV}. \tag{11}$$

At this point, the elastic energy density ψ^{el} is split into two parts – a damaged part ψ^{d} on which a degradation function $g(d)$ acts, and an intact part ψ^{i}:

$$\psi^{\mathrm{el}} = \psi^{\mathrm{el}}(\varepsilon_{ij}, d) = g(d)\psi^{\mathrm{d}}(\varepsilon_{ij}) + \psi^{\mathrm{i}}(\varepsilon_{ij}). \tag{12}$$

This split is often motivated by the observation that the tensile strain components contribute to the damage process that results in fracture, while the compression strain components do not. Various forms of a split in the energy density ψ^{el} have been investigated by Amor et al. (2009).

The substitution of the expression for the smeared fracture energy, Eq. (11), into Eq. (8) must be complemented by a relation between the elastic energy density ψ^{el} and the phase-field variable d. This link is inspired by damage models where a degradation function $g(d)$ reduces the stiffness of the bulk of the solid. The degradation function g has to fulfil the following properties

- $g(0) = 1$, since for $d = 0$ no damage occurs;
- $g(1) = 0$, since for $d = 1$ the damaged part ψ^{d} has to vanish;
- $g'(0) \neq 0$, since the damage has to be initiated at the onset;
- $g'(1) = 0$, since the energy must converge to a finite value for the fully broken state,

see Braides (1998); Pham et al. (2011); Pham and Marigo (2013) for a general discussion. For the degradation function $g(d)$ use has often been made of the quadratic function (Miehe et al., 2010b):

$$g(d) = (1 - d)^2. \tag{13}$$

Borden (2012) has introduced a cubic degradation function, which results in force-displacement curves which better reflect the behaviour of brittle materials, as less damage occurs before reaching the peak load, see also Vignollet et al. (2014).

It is important to note that, while the crack has been smeared in Eq. (11) on purely mathematical grounds, the introduction of the degradation function $g(d)$ in Eq. (12) is heuristic, inspired by a phenomenological concept that is commonly used in damage mechanics. This detracts from the original mathematical elegance and purity of the formulation.

We now substitute Eqs (11), (12) and (13) into Eq. (8) to yield the potential Π_ℓ for a solid with a smeared crack:

$$\Pi_\ell = \int_\Omega \left((1-d)^2\psi^{\mathrm{d}} + \psi^{\mathrm{i}}\right) \mathrm{dV} + \int_\Omega \mathcal{G}_c \gamma_\ell \, \mathrm{dV}. \tag{14}$$

Γ-convergence (with $\psi^{\mathrm{d}} = \psi^{\mathrm{el}}$ and $\psi^{\mathrm{i}} = 0$) is then defined such that the functional Π_ℓ for the smeared crack converges to the discrete crack functional Π in Eq. (8) when $\ell \to 0$, i.e.

$$\Pi_\ell\big|_{\ell\to 0} = \left(\int_\Omega (1-d)^2\psi^{\mathrm{el}} \, \mathrm{dV} + \int_\Omega \mathcal{G}_c\gamma_\ell \, \mathrm{dV}\right)\Big|_{\ell\to 0} = \int_\Omega \psi^{\mathrm{el}} \, \mathrm{dV} + \int_\Gamma \mathcal{G}_c \, \mathrm{dA} = \Pi. \tag{15}$$

According to Chambolle (2004)

$$\Pi_\ell(u_\ell, d) = \int_\Omega ((1-d)^2 + \eta)\psi^{\mathrm{el}}(u_\ell) \, \mathrm{dV} + \int_\Omega \mathcal{G}_c\gamma_\ell(d) \, \mathrm{dV}, \tag{16}$$

with the stabilisation parameter η, Γ-converges for $\eta \to 0$ and $\ell \to 0$ ($\eta \ll \ell$) to:

$$\Pi(u) = \int_\Omega \psi^{\mathrm{el}}(u) \, \mathrm{dV} + \int_\Gamma \mathcal{G}_c \, \mathrm{dA} \tag{17}$$

if the global minimisers u_ℓ of Π_ℓ converge to the global minimisers u of Π. Furthermore, the Γ-convergence result of Bellettini and Coscia (1994) reads in the mechanical context: The discretised version $\Pi_{\ell,h}$ of Π_ℓ,

$$\Pi_{\ell,h}(u_{\ell,h}, d_h) = \int_\Omega ((1-d_h)^2 + \eta)\psi^{\mathrm{el}}(u_{\ell,h}) \, \mathrm{dV} + \int_\Omega \mathcal{G}_c\gamma_\ell(d_h) \, \mathrm{dV} \tag{18}$$

Γ-converges to Π for $\eta \to 0$, $\ell \to 0$ and $h \to 0$ ($\eta \ll \ell$, $h \ll \ell$). It is noted that in the simulations we have set $\eta = 0$, similar to Borden et al. (2012).

For a discrete medium, i.e. when the solid is discretised into linear finite elements, Bourdin et al. (2008) have argued that a correction factor must be applied that is approximately equal to $1 + \frac{h}{4\ell}$, so that the fracture energy in Eq. (14) is replaced by the expression:

$$\mathcal{G}_c \to \left(1 + \frac{h}{4\ell}\right)\mathcal{G}_c, \tag{19}$$

see also Borden et al. (2014) where this correction has been considered in numerical studies of Γ-convergence for second and fourth-order phase-field models. In that study Γ-convergence was obtained numerically for prescribed displacement fields, which is different from the present study, where the displacement fields evolve from computations of a non-linear problem, and are thus fully compatible with the equilibrium equations, the kinematic equations, and the constitutive formulation.

We note that in practical computations the strict condition $h \ll \ell$ can be difficult to fulfill, especially since the length scale parameter ℓ already needs to be small in order to resolve the crack properly. In numerical simulations the weaker condition $h < l$ is often adopted (Piero et al., 2007; Bourdin, 2007; Bourdin et al., 2008; Amor et al., 2009; Miehe et al., 2010a; Kuhn and Müller, 2010; Borden et al., 2012, 2014).

For a given equilibrium configuration we minimise Π_ℓ and require the variation of Eq. (14) to be zero:

$$\delta\Pi_\ell = \frac{\partial\Pi_\ell}{\partial\varepsilon_{ij}}\delta\varepsilon_{ij} + \frac{\partial\Pi_\ell}{\partial d}\delta d + \frac{\partial\Pi_\ell}{\partial d_{,i}}\delta d_{,i} = 0. \tag{20}$$

Since $\delta\Pi_\ell = 0$ must hold for all admissible $\delta\varepsilon_{ij}$ and δd this leads to the following system of equations:

$$\sigma_{ij,i} = 0, \tag{21}$$

$$\frac{\mathcal{G}_c}{2\ell}(d - 4\ell^2\Delta d) + \frac{\partial g}{\partial d}\mathcal{H} = 0 \tag{22}$$

where the history parameter

$$\mathcal{H} = \max \psi^{\mathrm{d}} \tag{23}$$

ensures irreversibility in the sense that cracks can only grow ($\dot{d} \geq 0$) (Miehe et al., 2010a) for $\psi^{\mathrm{d}} \to \infty$. Alternatively, in Bourdin *et al.* (2008), irreversibility has been enforced by setting $d = 1$ when d becomes close to one. The term $\frac{\partial g}{\partial d}\mathcal{H}$ in Eq. (22) can be interpreted as the driving force for damage evolution and ensures that $d \to 1$ for $\psi^{\mathrm{d}} \to \infty$. From Eq. (21) the stress σ_{ij} is defined as:

$$\sigma_{ij} = \frac{\partial\psi^{\mathrm{el}}}{\partial\varepsilon_{ij}} = g(d)\frac{\partial\psi^{\mathrm{d}}}{\partial\varepsilon_{ij}} + \frac{\partial\psi^{\mathrm{i}}}{\partial\varepsilon_{ij}}. \tag{24}$$

The system Eq. (21) – Eq. (22) is complemented by the boundary conditions:

$$\sigma_{ij}n_j = \bar{t}_i \text{ on } \partial\Omega_t, \tag{25}$$

$$u_i = \bar{u}_i \text{ on } \partial\Omega_u, \tag{26}$$

$$d_{,i}n_i = 0 \text{ on } \partial\Omega \tag{27}$$

with $\partial\Omega_t \cap \partial\Omega_u = \emptyset$, $\partial\Omega_t \cup \partial\Omega_u = \partial\Omega$, the prescribed surface traction $\bar{\boldsymbol{t}}$ and prescribed displacement $\bar{\boldsymbol{u}}$.

3.2. Finite element formulation for the phase-field model for brittle fracture

We discretise the domain Ω into E elements, $\Omega = \bigcup_{e=1}^{E}\Omega^e$, and approximate the field variables and their derivatives,

$$d^e = \underline{\boldsymbol{N}}_d^T\underline{\boldsymbol{d}}, \quad \delta d^e = \underline{\boldsymbol{N}}_d^T\delta\underline{\boldsymbol{d}}, \quad \underline{\boldsymbol{d}}_{,i}^e = \underline{\underline{\mathbf{B}}}_d\underline{\boldsymbol{d}}, \quad \delta\underline{\boldsymbol{d}}_{,i}^e = \underline{\underline{\mathbf{B}}}_d\delta\underline{\boldsymbol{d}}, \tag{28}$$

$$\underline{\boldsymbol{u}}^e = \underline{\underline{\mathbf{N}}}_u\underline{\boldsymbol{u}}, \quad \delta\underline{\boldsymbol{u}}^e = \underline{\underline{\mathbf{N}}}_u\delta\underline{\boldsymbol{u}}, \quad \underline{\boldsymbol{\varepsilon}}^e = \underline{\underline{\mathbf{B}}}_u\underline{\boldsymbol{u}}, \quad \delta\underline{\boldsymbol{\varepsilon}}^e = \underline{\underline{\mathbf{B}}}_u\delta\underline{\boldsymbol{u}}, \tag{29}$$

where $\underline{\boldsymbol{N}}_d$ and $\underline{\underline{\mathbf{N}}}_u$ contain the interpolation functions of the phase field and the displacement field, respectively, and $\underline{\underline{\mathbf{B}}}_d$ and $\underline{\underline{\mathbf{B}}}_u$ contain their derivatives. Then, the weak forms in Eqs (21) and (22) result in the following matrix-vector equation:

$$\delta\underline{\boldsymbol{u}}^T \underbrace{\int_\Gamma \underline{\underline{\mathbf{N}}}_u^T \underline{\boldsymbol{t}}\, \mathrm{dA}}_{\underline{\boldsymbol{f}}_u^{\mathrm{ext}}} - \delta\underline{\boldsymbol{u}}^T \underbrace{\int_\Omega \underline{\underline{\mathbf{B}}}_u^T (g\underline{\underline{\mathbf{C}}}^{\mathrm{d}} + \underline{\underline{\mathbf{C}}}^{\mathrm{i}})\underline{\underline{\mathbf{B}}}_u \underline{\boldsymbol{u}}\, \mathrm{dV}}_{\underline{\boldsymbol{f}}_u^{\mathrm{int}}(\underline{\boldsymbol{d}},\underline{\boldsymbol{u}})} = 0, \tag{30}$$

$$\delta\underline{\boldsymbol{d}}^T \underbrace{\int_\Omega \frac{\mathcal{G}_c}{2\ell}\left(\underline{\underline{\mathbf{N}}}_d^T \underline{\underline{\mathbf{N}}}_d + 4\ell^2 \underline{\underline{\mathbf{B}}}_d^T \underline{\underline{\mathbf{B}}}_d\right)\underline{\boldsymbol{d}} + \underline{\boldsymbol{N}}_d^T \frac{\partial g}{\partial d}\mathcal{H}\, \mathrm{dV}}_{\underline{\boldsymbol{f}}_d^{\mathrm{int}}(\underline{\boldsymbol{d}},\underline{\boldsymbol{u}})} = 0 \tag{31}$$

where $\underline{\underline{\mathbf{C}}}^{\mathrm{d}}$ corresponds to the damaged part of the elasticity matrix, $\underline{\underline{\mathbf{C}}}^{\mathrm{i}}$ to the intact part of the elasticity matrix, and $\underline{\boldsymbol{f}}_d^{\mathrm{int}}(\underline{\boldsymbol{d}},\underline{\boldsymbol{u}})$ is the internal force vector related to the phase field. Introducing an arc-length method to control the loading process as in Verhoosel et al. (2009) and May et al. (2014), we can parameterise the external load vector as $\tilde{\underline{\boldsymbol{f}}}_u^{\mathrm{ext}} = \lambda\hat{\underline{\boldsymbol{f}}}$, with $\hat{\underline{\boldsymbol{f}}}$ a normalised external force vector, and λ a load parameter. Requiring Eq. (30) to hold for any kinematically admissible $\delta\underline{\boldsymbol{u}}$, this equation then transforms into:

$$\lambda\hat{\underline{\boldsymbol{f}}} - \underline{\boldsymbol{f}}_u^{\mathrm{int}}(\underline{\boldsymbol{d}},\underline{\boldsymbol{u}}) = \underline{\mathbf{0}}, \tag{32}$$

with $\underline{\boldsymbol{f}}_u^{\mathrm{int}}(\underline{\boldsymbol{d}},\underline{\boldsymbol{u}})$ the internal force vector related to the mechanical field problem. In the examples presented in the remainder of this paper the arc-length technique introduced in May et al. (2014) has been used to trace the equilibrium path. This arc-length function switches automatically between the rate of internal energy $\dot{\mathcal{U}}$ and the rate of dissipated energy $\dot{\mathcal{E}}^D$, depending on which measure is the more appropriate for that part of the equilibrium path. Denoting the arc-length function by φ the following system of equations must be solved:

$$\underline{\boldsymbol{h}}(\underline{\boldsymbol{d}},\underline{\boldsymbol{u}},\lambda) = \begin{bmatrix} \underline{\boldsymbol{f}}_d^{\mathrm{int}}(\underline{\boldsymbol{d}},\underline{\boldsymbol{u}}) \\ \underline{\boldsymbol{f}}_u^{\mathrm{int}}(\underline{\boldsymbol{d}},\underline{\boldsymbol{u}}) - \lambda\hat{\underline{\boldsymbol{f}}} \\ \varphi(\underline{\boldsymbol{u}},\lambda) \end{bmatrix} = \underline{\mathbf{0}}. \tag{33}$$

Linearisation of Eq. (33) yields the solution at iteration $i+1$ in the increment n:

$$\begin{bmatrix} \underline{\boldsymbol{d}} \\ \underline{\boldsymbol{u}} \\ \lambda \end{bmatrix}_{i+1}^{n} = \begin{bmatrix} \underline{\boldsymbol{d}} \\ \underline{\boldsymbol{u}} \\ \lambda \end{bmatrix}_{i}^{n} - \underline{\underline{\mathbf{K}}}_T^{-1}\Big|_i^n \cdot \begin{bmatrix} \underline{\boldsymbol{f}}_d^{\mathrm{int}}(\underline{\boldsymbol{d}},\underline{\boldsymbol{u}}) \\ \underline{\boldsymbol{f}}_u^{\mathrm{int}}(\underline{\boldsymbol{d}},\underline{\boldsymbol{u}}) - \lambda\hat{\underline{\boldsymbol{f}}} \\ \varphi(\underline{\boldsymbol{u}},\lambda) \end{bmatrix}_i^n \tag{34}$$

with

$$\underline{\underline{\mathbf{K}}}_T(\underline{\boldsymbol{d}},\underline{\boldsymbol{u}},\lambda) = \begin{bmatrix} \dfrac{\partial \underline{\boldsymbol{f}}_d^{\mathrm{int}}(\underline{\boldsymbol{d}},\underline{\boldsymbol{u}})}{\partial \underline{\boldsymbol{d}}} & \dfrac{\partial \underline{\boldsymbol{f}}_d^{\mathrm{int}}(\underline{\boldsymbol{d}},\underline{\boldsymbol{u}})}{\partial \underline{\boldsymbol{u}}} & \underline{\mathbf{0}} \\ \dfrac{\partial \underline{\boldsymbol{f}}_u^{\mathrm{int}}(\underline{\boldsymbol{d}},\underline{\boldsymbol{u}})}{\partial \underline{\boldsymbol{d}}} & \dfrac{\partial \underline{\boldsymbol{f}}_u^{\mathrm{int}}(\underline{\boldsymbol{d}},\underline{\boldsymbol{u}})}{\partial \underline{\boldsymbol{u}}} & -\hat{\underline{\boldsymbol{f}}} \\ \underline{\mathbf{0}}^T & \dfrac{\partial \varphi(\underline{\boldsymbol{u}},\lambda)}{\partial \underline{\boldsymbol{u}}} & \dfrac{\partial \varphi(\underline{\boldsymbol{u}},\lambda)}{\partial \lambda} \end{bmatrix}. \tag{35}$$

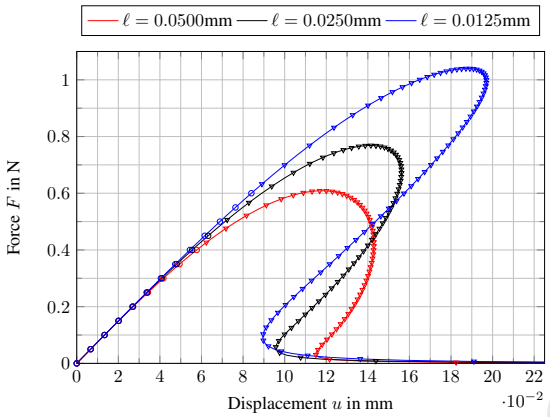

Figure 2: Results for a simple tensile test with a brittle phase-field model for a varying length scale ℓ

3.3. Phase field models for brittle fracture: a numerical assessment

We first summarise the main results from Vignollet et al. (2014) for a one-dimensional bar under tension using the phase-field model for brittle fracture:

- A decreasing length scale parameter ℓ results in a higher peak force, Fig. 2. Furthermore, a smaller length scale parameter ℓ results in a more pronounced snap-back behaviour. Pham et al. (2011); Borden et al. (2012) and Pham and Marigo (2013) also state that the length scale parameter ℓ in the model by Bourdin et al. (2000) can be interpreted as a material parameter since it influences the critical stress. This makes it less straightforward to decide how ℓ should be handled in phase-field models for brittle fracture. While the parameter ℓ has originally been introduced mathematically for the (smeared) approximation of a sharp crack, numerical experiments show that it attains the character of a material parameter.

- When using a cubic degradation function Borden (2012) a more linear behaviour is obtained at the beginning of loading, and the snap-back behaviour becomes sharper. However, the cubic degradation function comes at the expense of the introduction of an additional parameter s which again influences the behaviour of the force-displacement curve.

- A staggered approach as in Miehe et al. (2010b), which does not invoke an iteration loop between both fields for each step, is not able to capture snap-back behaviour since it essentially uses a displacement control. The staggered approach is robust in the sense that a solution is always obtained, but this solution does not necesarily represent an equilibrium state. The only rigorous manner to obtain a converged equilibrium solution is to use a monolithic scheme, or a staggered scheme with an iteration loop in each step between both fields.

In view of the above observations, the phase-field model for brittle fracture should rather be treated as a damage model: the degradation function $g(d)$ is motivated from damage mechanics and the differential equation in Eq. (22) is, in fact, an equation

which describes the evolution of d, very similar to the differential equation for the damage variable in gradient damage models (Peerlings et al., 1996).

In the following, Γ-convergence will be checked numerically by examining the *final* crack length for the bar. We will also show that for a plate under shear loading different solutions can be obtained depending on how the boundary conditions are precisely imposed. In all examples the relation $\ell \geq h$, with ℓ the length scale parameter and h the mesh size has been adhered to (Miehe et al., 2010b), which in view of Fig. 1 implies that we have at least four linear elements over the central part of the smeared crack.

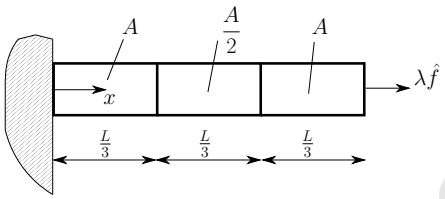

Figure 3: Bar with a reduced cross section subject to a tensile load $\lambda\hat{f}$

3.3.1. A one-dimensional bar with a reduced cross section under tension

We consider the one-dimensional bar depicted in Fig. 3. The bar has a reduced cross section in the centre part and the load $\lambda\hat{f}$ is applied to the right edge. The material parameters are $E = 10$ MPa for the Young's modulus, $\mathcal{G}_c = 0.1$ Nmm^{-1} for the fracture toughness, $L = 1$ mm for the length of the bar, $A = 1$ mm^2. Since only tensile stresses exist in this case, we can set $\psi^{\mathrm{i}} = 0$, while the quadratic degradation function $g(d) = (1-d)^2$ acts directly on the Young's modulus E, since $\psi^{\mathrm{d}} = \frac{1}{2}E\varepsilon^2$.

Now, a convergence study with respect to the *final* crack surface Γ_ℓ is carried out for this one-dimensional structure. The purpose is to check whether Γ_ℓ converges to Γ in a non-linear computation. The theoretical *final* crack surface for the bar of Fig. 3 is $\Gamma = A/2$, which is equal to the cross section of the segment in the centre of the bar. The numerically obtained *final* crack surface Γ_ℓ can be calculated using Eq. (5),

$$\Gamma_\ell = \int_\Omega \underbrace{\frac{1}{4\ell}\left(d^2 + 4\ell^2 d_{,x}{}^2\right)}_{\gamma_\ell} \,\mathrm{dV},$$

with Γ_ℓ evaluated when $\max d > 0.99$, and the error Γ_E is defined according to:

$$\Gamma_{\mathrm{E}} = \frac{|\Gamma_\ell - \Gamma|}{\Gamma}. \tag{36}$$

Fig. 4 gives the convergence study of the *final* crack surface Γ_ℓ when using the quadratic degradation function $g(d) = (1-d)^2$ for different values of the length scale parameter ℓ. Three different mesh sizes h have been used. Fig. 4 shows that all results for Γ_ℓ give a rather poor approximation of the theoretical *final* crack surface Γ, since invariably the error $\Gamma_{\mathrm{E}} > 0.1$. Below a certain value of the ratio ℓ/h, a further *decrease* results in an *increase* of the error Γ_{E}. Fig. 5 shows that this also holds when the correction of Eq. (19) for the fracture energy proposed by Bourdin et al. (2008) is taken into

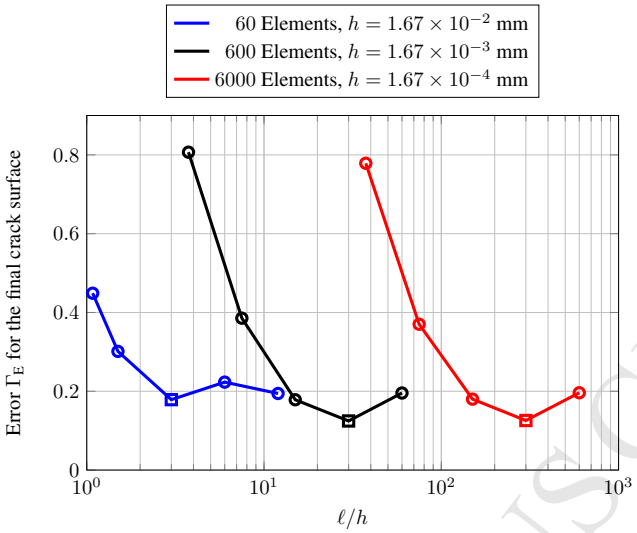

Figure 4: Convergence study for the *final* crack surface Γ_ℓ for a one-dimensional bar. The squares correspond to $\ell = 0.05$ mm.

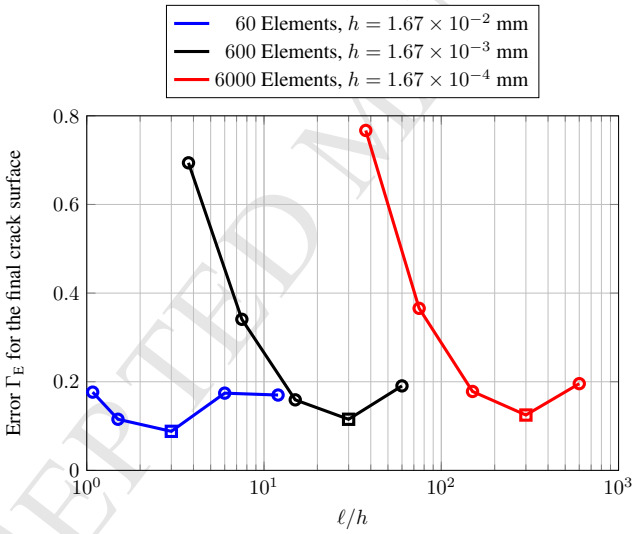

Figure 5: Convergence study for the *final* crack surface Γ_ℓ for a one-dimensional bar taking into account the correction Eq. (19) to the fracture energy proposed by Bourdin et al. (2008). The squares correspond to $\ell = 0.05$ mm.

account. The minimum occurs for the same values of the internal length scale ($\ell = 0.05$ mm). It is remarkable that for finer meshes the error Γ_E does not decrease.

Fig. 6 shows the evolution of the phase field in the course of the loading process for the mesh with 600 elements. The distribution seems to reasonably approximate the

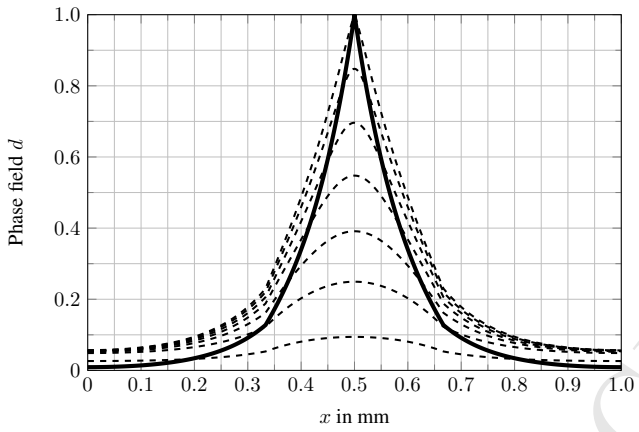

Figure 6: Evolution of the phase field variable d at various stages in the loading process (dashed black). The solid black curve represents the distribution for d when $d = 1$ is prescribed in the centre of the bar. The mesh size is $h = 1.67 \times 10^{-3}$mm for 600 elements and the length scale parameter is $\ell = 0.00625$.

theoretical profile. However, the phase-field variable becomes larger than the optimal profile, and the final profile is different from the optimal profile, rendering the energies associated with both profiles different.

The present numerical results indicate that, when the internal length scale $\ell \to 0$, the smeared crack length ceases to converge towards the true crack length in the phase-field models for brittle fracture. Indeed, it seems that for $\ell \to 0$:

$$\Pi_{\ell,h}\big|_{\ell\to 0} \neq \Pi \quad \text{since} \quad \Gamma_\ell\big|_{\ell\to 0} \neq \Gamma, \tag{37}$$

and Γ-convergence is not attained. Considering Fig. 5 it seems that for each discretisation, there is a range of ℓ/h-values for which Γ_{E} becomes minimal.

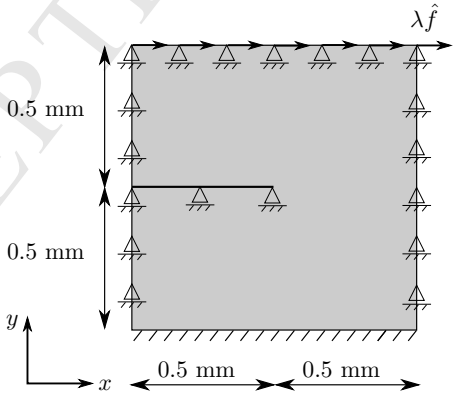

Figure 7: Plate under shear; the initial notch is modelled as a discrete crack

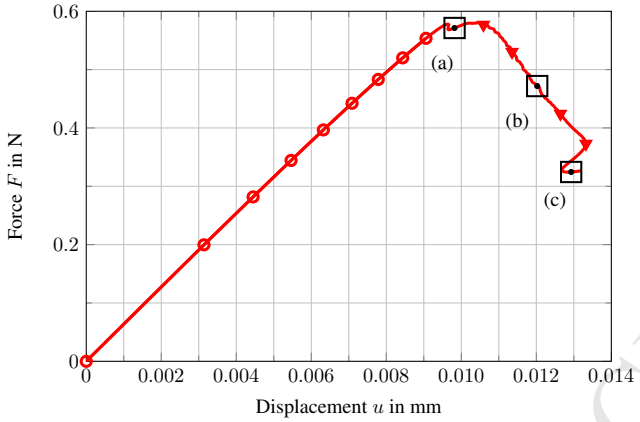

Figure 8: Force-displacement curve for the plate under shear when the initial notch is modelled as a discrete crack; the mesh consists of 100×100 elements, so that the mesh size is $h = 0.01$ mm; the length scale parameter is $\ell = 0.01$ mm

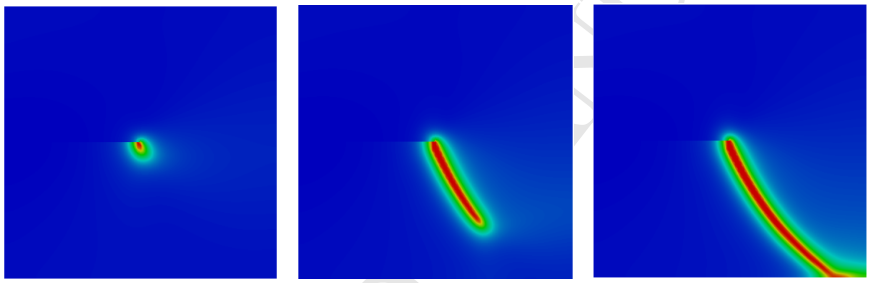

Figure 9: Propagation of the variable d for the plate under shear when the initial notch is modelled as a discrete crack; plots correspond to the squares in Fig. 8

3.3.2. Influence of the boundary conditions

The phase-field model for brittle fracture can give different results depending on how the boundary conditions are imposed. We consider the plate of Fig. 7, subjected to a shear load. For this reason, ψ^{d} contains contributions that stem from the tensile strains:

$$\psi^{\mathrm{d}} = \frac{1}{2}\lambda(\varepsilon_{ii}^{+})^2 + \mu\varepsilon_{ij}^{+}\varepsilon_{ij}^{+}, \tag{38}$$

and ψ^{i} contains those from the compressive strains:

$$\psi^{\mathrm{i}} = \frac{1}{2}\lambda(\varepsilon_{ii}^{-})^2 + \mu\varepsilon_{ij}^{-}\varepsilon_{ij}^{-}, \tag{39}$$

with ε_{ij}^{+}, ε_{ij}^{-} the positive and negative strain components that result from a spectral decomposition of $\boldsymbol{\varepsilon}$. The bottom edge is fixed in the x-direction. All edges are fixed in the y-direction.

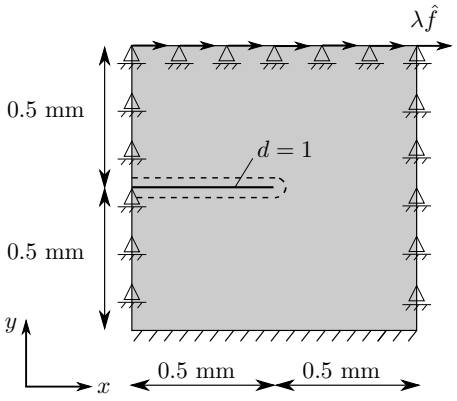

Figure 10: Plate under shear; the initial notch is modelled with $d = 1$

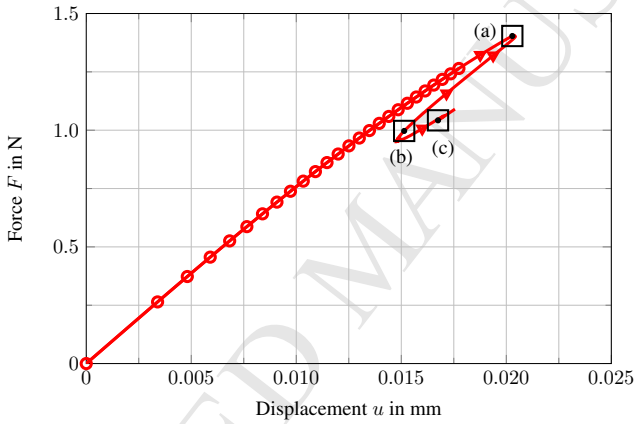

Figure 11: Force-displacement curve for the plate under shear when the initial notch modelled with $d = 1$; the mesh consists of 100×100 elements, so that the mesh size is $h = 0.01$ mm; the length scale parameter is $\ell = 0.01$ mm

The notch is first modelled in a discrete sense, by applying the boundary conditions shown in Fig. 7. The shear load $\lambda\hat{f}$ is applied at the top edge in the positive x-direction. The length scale parameter is $\ell = 0.01$ mm and the mesh size $h = 0.01$ mm for a mesh with 100×100 elements. The force-displacement curve and the evolution of the phase-field variable d are depicted in Fig. 8 and Fig. 9, respectively.

Next, the initial notch is introduced by prescribing $d = 1$, cf. Fig. 10. This should give the same results, since $d = 1$ represents the centre of the smeared notch. With this boundary condition, the force-displacement curve of Fig. 11 is obtained. The corresponding patterns for the propagation of the phase-field variable d are depicted in Fig. 12, and are very different from those in Fig. 9.

It is recognised that the applied boundary condition $d = 1$ derives from the as-

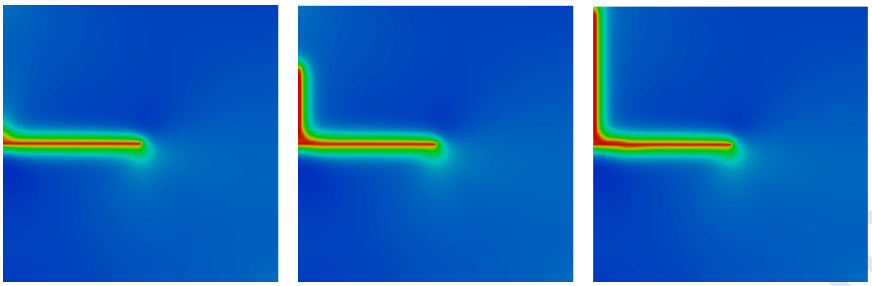

(a) (b) (c)

Figure 12: Propagation of the variable d for the plate under shear when the initial notch is modelled with $d = 1$; plots correspond to the squares in Fig. 11

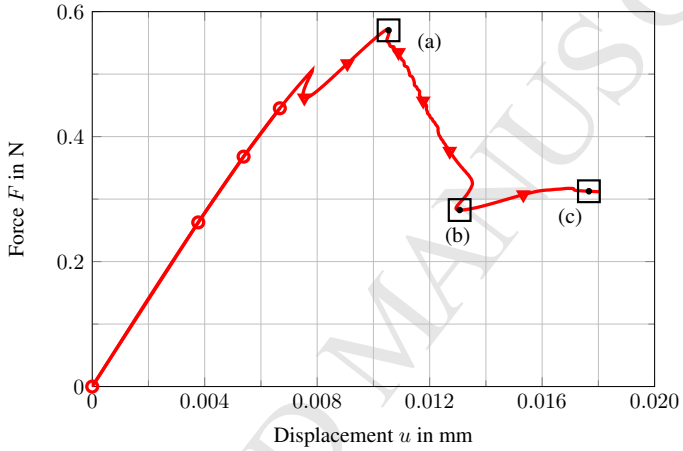

Figure 13: Force-displacement curve for the plate under shear when for the left half of the plate $\psi^{\mathrm{d}} = \psi^{\mathrm{el}}$ is set. The mesh consists of 100×100 elements, so that the mesh size is $h = 0.01$ mm; the length scale parameter is $\ell = 0.01$ mm. Squares correspond to the phase field distributions for d in Fig. 14.

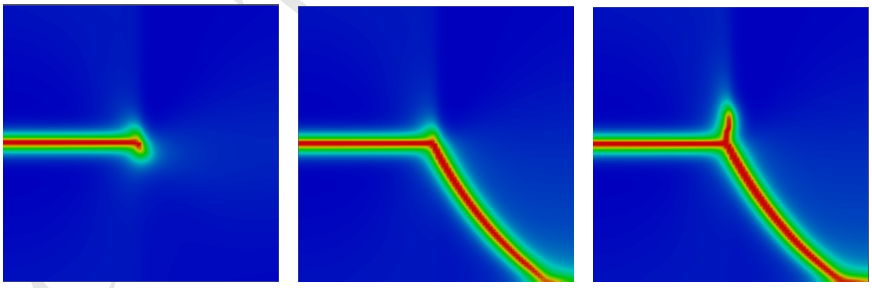

(a) (b) (c)

Figure 14: Propagation of the variable d for the plate under shear; plots correspond to the squares in Fig. 13

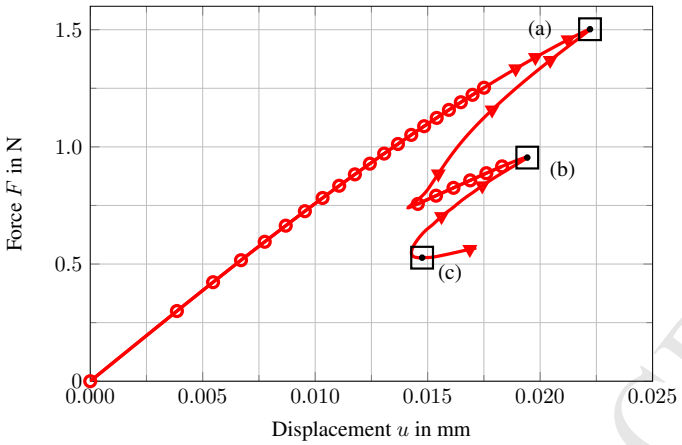

Figure 15: Force-displacement curve for the plate under shear when for the top left edge of the plate $d = 0$ is prescribed. The mesh consists of 100×100 elements, so that the mesh size is $h = 0.01$ mm; the length scale parameter is $\ell = 0.01$ mm. Squares correspond to the phase field distributions for d in Fig. 16.

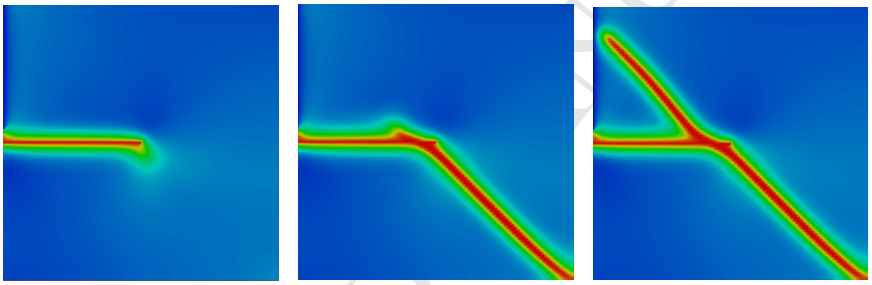

Figure 16: Propagation of the variable d for the plate under shear. The plots correspond to the squares in Fig. 15

sumption $\psi^{\mathrm{d}} = \psi^{\mathrm{d}}(\varepsilon_{ij}^{+})$. Different results are obtained, for instance, when assuming that: $\psi^{\mathrm{d}} = \psi^{\mathrm{el}}$, $\psi^{\mathrm{i}} = 0$ in the left part of the plate. The resulting force-displacement curves and the crack path are then in better agreement with the first calculation, i.e. when the notch is applied in a discrete sense, see Fig. 13 and Fig. 14, respectively. However, a secondary crack starts to propagate at a certain stage in the loading process. Moreover, it is not clear where $\psi^{\mathrm{d}} = \psi^{\mathrm{el}}$, $\psi^{\mathrm{i}} = 0$ should be prescribed, since the crack is smeared and also extends into the right part of the plate. A further calculation was carried out by prescribing $d = 0$ on the top left edge as suggested in Amor et al. (2009). The resulting force-displacement curve and crack path are again different from the case where the notch is modelled in a discrete sense, see Fig. 15 and 16. As in the previous case, a secondary crack emerges. Apparently, the phase-field model for brittle fracture is sensitive to the exact form of the applied boundary conditions, and boundary conditions which intuitively should give identical results, do not.

4. Phase field model for cohesive fracture

Verhoosel and de Borst (2013) have introduced a phase-field model for cohesive fracture. Promising results were obtained for decohesion along a predefined, straight interface. However, it appeared that care had to be exercised with respect to the proper interpolation of the independent variables, the displacements u_i, the phase-field variable d, and the crack opening field v_i. For one-dimensional examples it appeared that a cubic interpolation for u_i together with a linear interpolation for the other variables were sufficient to obtain a non-oscillatory stress field. In Vignollet et al. (2014) it was found that this observation did not carry over to unstructured meshes. After a brief recapitulation of the model, we will demonstrate the emergence of such stress oscillations for a simple, two-dimensional patch test, even for a properly balanced order of interpolation of the different independent variables.

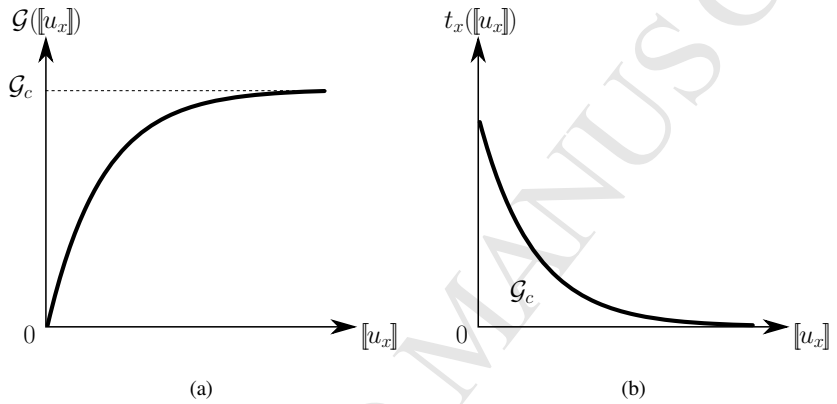

Figure 17: (a) Energy release $\mathcal{G}(\llbracket u_x \rrbracket)$ and (b) traction $t_x(\llbracket u_x \rrbracket)$ in the cohesive zone for the one-dimensional case

4.1. Continuum formulation for the phase-field model for cohesive fracture

For cohesive zone models the fracture energy $\mathcal{G}_c$ is released gradually and governed by the fracture energy function

$$\mathcal{G} = \mathcal{G}(\llbracket u_i \rrbracket). \tag{40}$$

The fracture energy function $\mathcal{G}$ depends on crack opening $\llbracket u_i \rrbracket$ at the interface and equals the fracture energy $\mathcal{G}_c$ at full crack opening, cf. Fig. 17(a). The traction t_i in the cohesive zone is evaluated as:

$$t_i(\llbracket u_j \rrbracket) = \frac{\partial \mathcal{G}(\llbracket u_j \rrbracket)}{\partial \llbracket u_i \rrbracket}, \tag{41}$$

see Fig. 17(b).

In the phase-field model for cohesive fracture, the crack is distributed over the solid, again by employing Eq. (5):

$$\int_\Gamma \mathcal{G}(\llbracket u_i \rrbracket)\, \mathrm{dA} = \int_\Omega \mathcal{G}(\llbracket u_i \rrbracket) \gamma_\ell \, \mathrm{dV}. \tag{42}$$

The spatial distribution in Eq. (42) should not affect $\mathcal{G}([\![u_i]\!])$ in the direction normal to the crack since, for any quantity $\mathcal{B}$,

$$\int_\Gamma \mathcal{B}\,\mathrm{dA} = \int_\Omega \mathcal{B}\gamma_\ell\,\mathrm{dV}. \tag{43}$$

The crack opening $[\![u_i]\!]$, and therefore $\mathcal{G}([\![u_i]\!])$, only exists at the crack surface Γ. For this reason, an auxiliary field v_i is introduced when distributing the crack, which is defined over the volume Ω. In view of Eq. (43), $\mathcal{G}(v_i)$ must not change in the direction normal to the crack, which requirement is satisfied when enforcing the following constraint on the auxiliary field v_i:

$$\frac{\partial v_i}{\partial n} = 0. \tag{44}$$

Evidently, v_i being constant in the direction normal to the crack implies that $\mathcal{G}(v_i)$ is constant as well. The expression for Eq. (42) thus becomes:

$$\int_\Gamma \mathcal{G}([\![u_i]\!])\,\mathrm{dA} = \int_\Omega \mathcal{G}(v_i)\gamma_\ell\,\mathrm{dV} \quad \text{subject to } \tfrac{\partial v_i}{\partial n} = 0. \tag{45}$$

It is noted that for brittle fracture $\mathcal{G}([\![u_i]\!]) = \mathcal{G}_c = $ constant, and the requirement that $\int_\Omega \mathcal{G}_c\gamma_\ell\,\mathrm{dV}$, see Eq. (11), remains constant in the direction normal to the crack is automatically satisfied.

The phase-field model for cohesive fracture assumes a split of the strain tensor into an elastic component and a component that accounts for damage:

$$\varepsilon_{ij} = \varepsilon^{\mathrm{el}}_{ij} + \varepsilon^{\mathrm{d}}_{ij} \tag{46}$$

such that in Eq. (9) ε_{ij} needs to be replaced by $\varepsilon^{\mathrm{el}}_{ij}$

$$\psi^{\mathrm{el}} = \psi^{\mathrm{el}}(\varepsilon^{\mathrm{el}}_{ij}) = \psi^{\mathrm{el}}\left(\varepsilon^{\mathrm{el}}_{ij}(d)\right) = \psi^{\mathrm{el}}(\varepsilon_{ij} - \varepsilon^{\mathrm{d}}_{ij}) \tag{47}$$

and

$$\sigma_{ij} = \frac{\partial \psi^{\mathrm{el}}}{\partial \varepsilon_{ij}} = \frac{\partial \psi^{\mathrm{el}}}{\partial \varepsilon^{\mathrm{el}}_{kl}}\frac{\partial \varepsilon^{\mathrm{el}}_{kl}}{\partial \varepsilon_{ij}} = \frac{\partial \psi^{\mathrm{el}}}{\partial \varepsilon^{\mathrm{el}}_{kl}}\delta_{ki}\delta_{lj} = \frac{\partial \psi^{\mathrm{el}}}{\partial \varepsilon^{\mathrm{el}}_{ij}}. \tag{48}$$

The tensor $\varepsilon^{\mathrm{d}}_{ij}$ that accounts for damage can be derived from thermodynamical considerations. The second law of thermodynamics gives (Jiràsek and Bažant, 2001):

$$\dot{\mathcal{D}} = \sigma_{ij}\dot{\varepsilon}_{ij} - \dot{\psi}^{\mathrm{el}} = \sigma_{ij}(\dot{\varepsilon}^{\mathrm{el}}_{ij} + \dot{\varepsilon}^{\mathrm{d}}_{ij}) - \frac{\partial \psi^{\mathrm{el}}}{\partial \varepsilon^{\mathrm{el}}_{ij}}\dot{\varepsilon}^{\mathrm{el}}_{ij} = \sigma_{ij}(\dot{\varepsilon}^{\mathrm{el}}_{ij} + \dot{\varepsilon}^{\mathrm{d}}_{ij}) - \sigma_{ij}\dot{\varepsilon}^{\mathrm{el}}_{ij} = \sigma_{ij}\dot{\varepsilon}^{\mathrm{d}}_{ij} \geq 0. \tag{49}$$

The dissipation $\dot{\mathcal{D}}$ for the distributed form in Eq. (45) can be evaluated explicitly from

$$\dot{\mathcal{D}} = \frac{\mathrm{d}}{\mathrm{dt}}(\gamma_\ell(d)\mathcal{G}(v_i)) = \mathcal{G}\frac{\partial \gamma_\ell}{\partial d}\dot{d} + \gamma_\ell\frac{\partial \mathcal{G}(v_j)}{\partial v_i}\dot{v}_i = \mathcal{G}\frac{\partial \gamma_\ell}{\partial d}\dot{d} + \gamma_\ell t_i \dot{v}_i. \tag{50}$$

The first term in Eq. (50) corresponds to the energy that is dissipated when advancing the cohesive zone by $\dot{d}$. Assuming that the smeared jump v_i is initially zero in the newly

created cohesive zone, the first term does not contribute to dissipation of energy, since $\mathcal{G}(0) = 0$, Fig. 17(a). The second term in Eq. (50) represents the energy dissipation as the result of further crack opening by $\dot{v}_i$. Substituting Eq. (50) into Eq. (49)

$$\gamma_\ell t_i \dot{v}_i = \sigma_{ij}\gamma_\ell \mathrm{sym}(\dot{v}_i n_j) = \sigma_{ij}\dot{\varepsilon}^{\mathrm{d}}_{ij} \tag{51}$$

yields $\varepsilon^{\mathrm{d}}_{ij}$, the contribution of the strain tensor that accounts for damage:

$$\varepsilon^{\mathrm{d}}_{ij} = \gamma_\ell \mathrm{sym}(v_i n_j). \tag{52}$$

It has been taken into account in Eq. (51) that the traction t_i in the smeared crack zone Γ_ℓ is also distributed over the solid and therefore $t_i = \sigma_{ij} n_j$. The potential of the phase-field model for cohesive fracture now reads:

$$\Pi_\ell = \int_\Omega \left(\psi^{\mathrm{el}}\, \mathrm{dV} + \mathcal{G}(v_i)\gamma_\ell + \frac{\alpha}{2}\left|\frac{\partial v_i}{\partial n}\right|^2 \right) \mathrm{dV} \tag{53}$$

where the last term has been introduced in order to enforce the smeared jump v_i to remain constant in the direction normal to the crack, cf. Eq. (44). Minimising Π_ℓ yields

$$\delta\Pi_\ell = \frac{\partial \Pi_l}{\partial \varepsilon^{\mathrm{el}}_{ij}}\delta\varepsilon^{\mathrm{el}}_{ij} + \frac{\partial \Pi_l}{\partial v_i}\delta v_i + \frac{\partial \Pi_l}{\partial\left(\frac{\partial v_i}{\partial n}\right)}\delta\left(\frac{\partial v_i}{\partial n}\right) + \frac{\partial \Pi_l}{\partial d_{,i}}\delta d_{,i} + \frac{\partial \Pi_l}{\partial d}\delta d = 0 \tag{54}$$

and the following equations result:

$$\sigma_{ij,i} = 0 \qquad \text{in } \Omega, \tag{55}$$

$$\gamma_\ell[t_i(v_j) - \sigma_{ij} n_j] = \alpha \frac{\partial^2 v_i}{\partial n^2} \qquad \text{in } \Gamma_\ell \tag{56}$$

subject to the boundary conditions

$$\sigma_{ij} n_j = \bar{t}_i \text{ on } \partial\Omega_h, \tag{57}$$

$$u_i = \bar{u}_i \text{ on } \partial\Omega_u, \tag{58}$$

$$\frac{\partial v_i}{\partial n} = 0 \text{ on } \partial\Gamma_\ell. \tag{59}$$

4.2. Finite element formulation for the phase-field model for cohesive fracture

The finite element formulation for the weak form of Eq. (55) and Eq. (56) is obtained after discretisation $\Omega = \bigcup_{e=1}^{E} \Omega^e$ and approximation of the field variables and their derivatives,

$$\underline{\boldsymbol{u}}^e = \underline{\underline{\mathbf{N}}}_u \underline{\boldsymbol{u}}, \quad \delta\underline{\boldsymbol{u}}^e = \underline{\underline{\mathbf{N}}}_u \delta\underline{\boldsymbol{u}}, \quad \underline{\boldsymbol{\varepsilon}}^e = \underline{\underline{\mathbf{B}}}_u \underline{\boldsymbol{u}}, \quad \delta\underline{\boldsymbol{\varepsilon}}^e = \underline{\underline{\mathbf{B}}}_u \delta\underline{\boldsymbol{u}}, \tag{60}$$

$$\underline{\boldsymbol{v}}^e = \underline{\underline{\mathbf{N}}}_v \underline{\boldsymbol{v}}, \quad \delta\underline{\boldsymbol{v}}^e = \underline{\underline{\mathbf{N}}}_v \delta\underline{\boldsymbol{v}}, \quad [\mathrm{sym}(\underline{\boldsymbol{v}} \otimes \underline{\boldsymbol{n}})]^e = \underline{\underline{\mathbf{B}}}_v \underline{\boldsymbol{v}}, \tag{61}$$

$$[\mathrm{sym}(\delta\underline{\boldsymbol{v}} \otimes \underline{\boldsymbol{n}})]^e = \underline{\underline{\mathbf{B}}}_v \delta\underline{\boldsymbol{v}}, \quad \left[\frac{\partial \underline{\boldsymbol{v}}}{\partial \underline{\boldsymbol{n}}}\right]^e = \underline{\underline{\mathbf{G}}}_v \underline{\boldsymbol{v}}, \quad \left[\frac{\partial \delta\underline{\boldsymbol{v}}}{\partial \underline{\boldsymbol{n}}}\right]^e = \underline{\underline{\mathbf{G}}}_v \delta\underline{\boldsymbol{v}}, \tag{62}$$

the following vector-matrix equation is obtained:

$$\delta\underline{\boldsymbol{u}}^T \underbrace{\int_\Omega \underline{\underline{\mathbf{N}}}_u^T \underline{\boldsymbol{h}}\,\mathrm{dA}}_{\underline{\tilde{\boldsymbol{f}}}_u^{\mathrm{ext}}} - \delta\underline{\boldsymbol{u}}^T \underbrace{\int_\Omega \underline{\underline{\mathbf{B}}}_u^T (\underline{\underline{\mathbf{C}}}\,\underline{\underline{\mathbf{B}}}_u\underline{\boldsymbol{u}} - \gamma_\ell \underline{\underline{\mathbf{C}}}\,\underline{\underline{\mathbf{B}}}_v\underline{\boldsymbol{v}})\,\mathrm{dV}}_{\underline{\boldsymbol{f}}_u^{\mathrm{int}}(\underline{\boldsymbol{v}},\underline{\boldsymbol{u}})} = 0 \tag{63}$$

$$\delta\underline{\boldsymbol{v}}^T \underbrace{\int_\Omega -\gamma_\ell \underline{\underline{\mathbf{B}}}_v^T (\underline{\underline{\mathbf{C}}}\,\underline{\underline{\mathbf{B}}}_u\underline{\boldsymbol{u}} - \gamma_\ell \underline{\underline{\mathbf{C}}}\,\underline{\underline{\mathbf{B}}}_v\underline{\boldsymbol{v}}) + \gamma_\ell \underline{\underline{\mathbf{N}}}_v^T \underline{\boldsymbol{t}} + \alpha \underline{\underline{\mathbf{G}}}_v^T \underline{\underline{\mathbf{G}}}_v \underline{\mathbf{v}}\,\mathrm{dV}}_{\underline{\boldsymbol{f}}_v^{\mathrm{int}}(\underline{\boldsymbol{v}},\underline{\boldsymbol{u}})} = 0, \tag{64}$$

with $\underline{\underline{\mathbf{C}}}$ the elasticity matrix. In the numerical cases studies of Section 4.3 it is sufficient to consider a single loading step under displacement control. Considering that the system of Eqs (63) – (64) must hold for any $(\delta\underline{\boldsymbol{u}}, \delta\underline{\boldsymbol{v}})$, and that the external forces vanish, $\bar{\underline{\boldsymbol{t}}} = \underline{\mathbf{0}}$ yields:

$$\underline{\boldsymbol{H}}(\underline{\boldsymbol{v}},\underline{\boldsymbol{u}}) = \begin{bmatrix} \underline{\boldsymbol{f}}_v^{\mathrm{int}}(\underline{\boldsymbol{v}},\underline{\boldsymbol{u}}) \\ \underline{\boldsymbol{f}}_u^{\mathrm{int}}(\underline{\boldsymbol{v}},\underline{\boldsymbol{u}}) \end{bmatrix} = \underline{\mathbf{0}}. \tag{65}$$

Linearisation of Eq. (65) yields the solution for iteration $i+1$:

$$\begin{bmatrix} \underline{\boldsymbol{v}} \\ \underline{\boldsymbol{u}} \end{bmatrix}_{i+1} = \begin{bmatrix} \underline{\boldsymbol{v}} \\ \underline{\boldsymbol{u}} \end{bmatrix}_i - \underline{\underline{\mathbf{K}}}_T^{-1}\Big|_i \cdot \begin{bmatrix} \underline{\boldsymbol{f}}_v^{\mathrm{int}}(\underline{\boldsymbol{v}},\underline{\boldsymbol{u}}) \\ \underline{\boldsymbol{f}}_v^{\mathrm{int}}(\underline{\boldsymbol{v}},\underline{\boldsymbol{u}}) \end{bmatrix}_i \tag{66}$$

with the tangent stiffness matrix:

$$\underline{\underline{\mathbf{K}}}_T(\underline{\boldsymbol{v}},\underline{\boldsymbol{u}}) = \begin{bmatrix} \dfrac{\partial \underline{\boldsymbol{f}}_v^{\mathrm{int}}(\underline{\boldsymbol{v}},\underline{\boldsymbol{u}})}{\partial \underline{\boldsymbol{v}}} & \dfrac{\partial \underline{\boldsymbol{f}}_v^{\mathrm{int}}(\underline{\boldsymbol{v}},\underline{\boldsymbol{u}})}{\partial \underline{\boldsymbol{u}}} \\ \dfrac{\partial \underline{\boldsymbol{f}}_u^{\mathrm{int}}(\underline{\boldsymbol{v}},\underline{\boldsymbol{u}})}{\partial \underline{\boldsymbol{v}}} & \dfrac{\partial \underline{\boldsymbol{f}}_u^{\mathrm{int}}(\underline{\boldsymbol{v}},\underline{\boldsymbol{u}})}{\partial \underline{\boldsymbol{u}}} \end{bmatrix}. \tag{67}$$

4.3. Numerical examples for the phase-field model for cohesive fracture

In what follows, a constant phase field d is considered, i. e. an interface is modelled. For this purpose a one-dimensional bar is considered with an elastic interface, Fig. 18. First, the bar is modelled with one-dimensional bar elements. The Young's modulus is $E = 10$ MPa, the stiffness of the interface $k = 10\,\mathrm{Nmm}^{-3}$, the length $L = 1$ mm and the length scale parameter is $\ell = L/10$. The penalty parameter is set $\alpha = 1$, and $d = 1$ is prescribed at the elastic interface, i. e. at the node in the centre of the bar. Different from Verhoosel and de Borst (2013) $d = 1$ is not prescribed at the Gauss points, since this can lead to $d > 1$ at the nodes (Vignollet et al., 2014). The bar consists of 10 elements with 5 elements in each segment, so that the mesh size is $h = 0.1$ mm. The prescribed displacement is $\bar{u}_x = 0.1$ mm.

Application of linear shape functions for the displacement u_x, the smeared jump v_x and the phase field d results in stress oscillations, Fig. 19(a), as was also observed

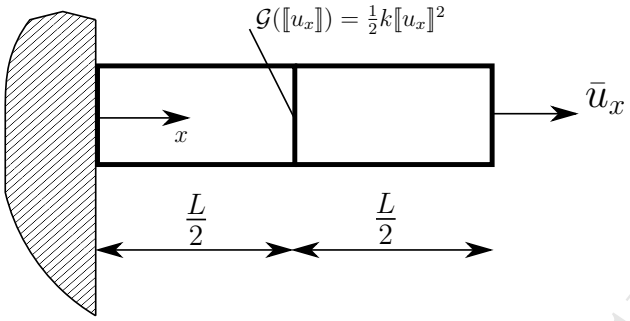

Figure 18: Bar with an elastic interface $\mathcal{G} = \frac{1}{2}k[\![u_x]\!] = \frac{1}{2}kv_x^2$ in the centre; with Eq. (41) the cohesive traction becomes $t_x = k[\![u_x]\!] = kv_x$

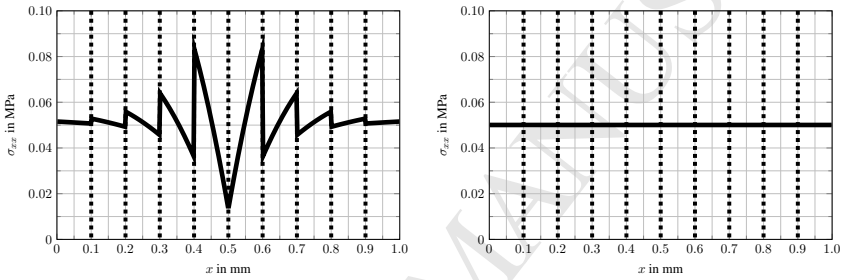

Figure 19: Stress distribution along the bar in Fig. 18 for (a) linear shape functions for u_x, v_x, d and (b) cubic shape functions for u_x and linear shape functions for v_x, d; the dashed lines mark element boundaries

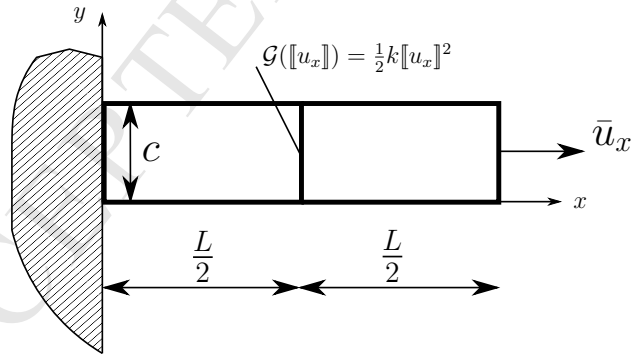

Figure 20: Bar from Fig. 18 in a two-dimensional setting with $\nu = 0$ and all $v_y = 0$

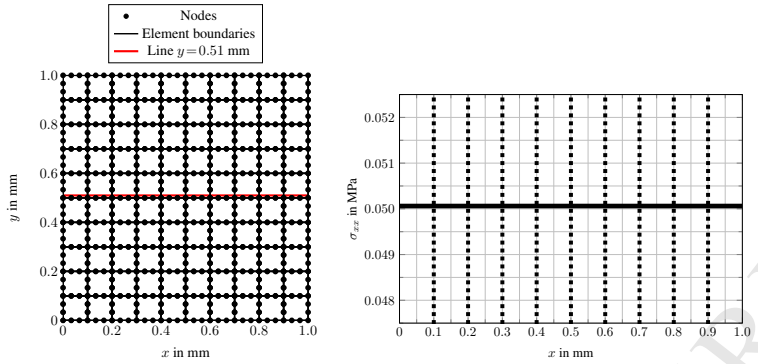

(a) (b)

Figure 21: For the structured mesh in (a) no stress oscillations are observed along the line $y = 0.51$ mm in (b). Dashed lines mark element boundaries.

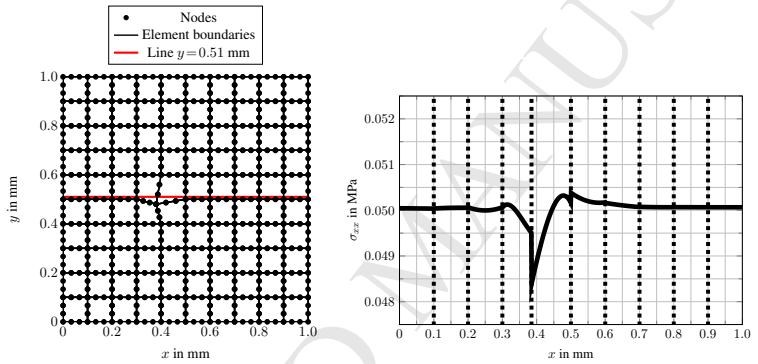

(a) (b)

Figure 22: For the unstructured mesh in (a) stress oscillations can be observed along the line $y=0.51$ mm in (b). Dashed lines correspond to element boundaries.

by Verhoosel and de Borst (2013). In one dimension, Eq. (46) can be rewritten using Eq. (5) as follows:

$$\varepsilon_{xx}^{\mathrm{el}} = \varepsilon_{xx} - \varepsilon_{xx}^{\mathrm{d}} = \frac{\mathrm{d}u_x}{\mathrm{d}x} - \gamma_\ell v_x = \frac{\mathrm{d}u_x}{\mathrm{d}x} - \frac{1}{4\ell}(d^2 + 4\ell^2 {d_{,x}}^2)v_x. \tag{68}$$

Since v_x is enforced to be constant, the strain $\varepsilon_{xx}^{\mathrm{d}}$ that accounts for damage has a quadratic distribution when linear shape functions are used for d. Therefore, the total strain ε_{xx} must have a quadratic distribution as well. This can be achieved when cubic shape functions are used for the displacement u_x. Fig. 19(b) shows that this is a successful remedy.

Keeping the interpolation of the displacement of the third order while those for the phase field and the crack opening remain linear, the bar is now reconsidered in a two-dimensional setting by putting Poisson's ratio $\nu = 0$ and by prescribing all $v_y = 0$, see

Fig. 20. A structured mesh with 10×10 elements is used. The width is $c = 1$ mm and $d = 1$ is prescribed at all nodes for which $x = L/2$. The other parameters are the same as in the purely one-dimensional case. Along the line $y = 0.51$ mm the same results are obtained for the stress distribution σ_{xx} as in case of the purely one-dimensional study, see Fig. 21. No stress oscillations are observed.

Next, the nodes are slightly displaced in a patch of four elements, Fig. 22(a), and stress oscillations result along the line $y = 0.51$ mm, see Fig. 22(b). This is in agreement with the results obtained in Vignollet et al. (2014), where the use of unstructured meshes for a peel test also resulted in stress oscillations. The present simulation can be considered as a patch test, since a homogeneous stress state should be obtained when prescribing a uniform traction or displacement at the boundary, irrespective of the mesh lay-out. Unfortunately, this is not obtained for the present three-field formulation of the cohesive phase-field fracture model.

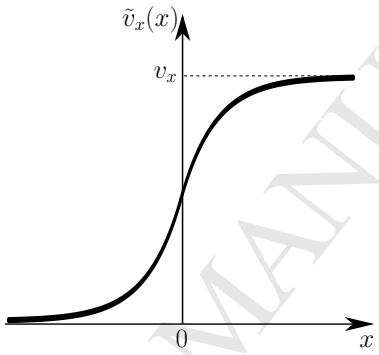

Figure 23: Non-constant jump $\tilde{v}_x(x)$

There are some possible explanations for the traction oscillations. First, we consider the total strain ε_{xx} from Eq. (46) in a one-dimensional format:

$$\varepsilon_{xx} = \frac{\mathrm{d}u_x}{\mathrm{d}x} = \varepsilon_{xx}^{\mathrm{el}} + \varepsilon_{xx}^{\mathrm{d}} = \frac{\mathrm{d}u_x^{\mathrm{el}}}{\mathrm{d}x} + \gamma_\ell v_x. \tag{69}$$

with the elastic displacement u_x^{el}. Integrating Eq. (69) with a constant smeared jump in the normal direction, $\frac{\partial v_x}{\partial x} = 0$, yields:

$$u_x(x) = u_x^{\mathrm{el}}(x) + \underbrace{v_x \int_{-\infty}^{x} \gamma_\ell(\tilde{x})\,\mathrm{d}\tilde{x}}_{\tilde{v}_x(x)}. \tag{70}$$

The integral in Eq. (70) can be interpreted as a smeared Heaviside step function $\mathcal{H}$ which is used in partition of unity approaches

$$u_x(x) = u_x^{\mathrm{el}}(x) + \mathcal{H} v_x(x). \tag{71}$$

It has been derived in Eq. (45) that the smeared jump field v_x needs to be constant in the normal direction to the crack in order to have a constant $\mathcal{G}(v_x)$ in the direction

normal to the crack. However, when the second term $\tilde{v}_x$ in Eq. (70) is interpreted as the jump for the smeared model, it is observed that this term is not constant in the normal direction to the crack, see also Fig. 23. Hence, there are two different interpretations for the smeared jump in the phase field model for cohesive fracture, v_x and $\tilde{v}_x$. Both interpretations cannot hold simultaneously, and the phase field model for cohesive fracture seems to embody a contradiction.

The different orders of the polynomials may also contribute to the oscillatory results. The distribution for the stress

$$\sigma_{xx} = E\varepsilon^{\mathrm{el}}_{xx} \tag{72}$$

is quadratic when cubic shape functions are used for the displacement field u and linear shape functions for the smeared jump v and the phase field d in Eq. (68). Since the cohesive traction is constant,

$$t_x = k[\![u_x]\!] = kv_x, \tag{73}$$

due to a constant v_x, it may be that the different orders of approximation for t_x (constant) and for σ_{xx} (quadratic) in Eq. (56) contribute adversely.

5. Concluding remarks

Phase-field models have recently found widespread popularity for simulating brittle crack propagation in a smeared manner. It has been shown that a number of phenomena that are difficult to capture in discrete crack models, like crack branching, can evolve naturally in a phase-field framework (Amor et al., 2009; Kuhn and Müller, 2010; Miehe et al., 2010a,b; Borden et al., 2012, 2014). Moreover, an extension to cohesive fracture has been made (Verhoosel and de Borst, 2013). However, concerns have been raised as well. In Vignollet et al. (2014) it has been shown that the load-displacement curves can depend considerably on the internal length scale ℓ that defines the width of the distributed fracture zone, and on the degradation function $g(d)$ that has been introduced in brittle phase-field models to link the elastic energy ψ^{el} to the phase-field variable d. Originally introduced in a mathematical sense as a perturbation parameter, it appears that the length scale ℓ takes on the role of a material parameter, quite similar to the internal length scale parameter in gradient plasticity or gradient damage models (de Borst and Mühlhaus, 1992; Peerlings et al., 1996). The same holds for the degradation function $g(d)$, which turns out to have the physical meaning of a material degradation function.

Another issue is whether the functional $\Pi_{\ell,h}$ for the discretised phase-field model for brittle fracture converges to Π when the internal length parameter $\ell \to 0$. In Chambolle (2004) mathematical arguments have been given that this is the case for a continuous medium, and Bourdin et al. (2008) have shown that for a discretised medium a correction factor has to be applied with respect to the fracture energy $\mathcal{G}_c$. Herein, we have shown by a one-dimensional example that Γ-convergence is not necessarily attained, since numerically the smeared crack length Γ_ℓ does not seem to converge to the discrete crack length Γ.

Finally, the cohesive fracture phase-field approach of Verhoosel and de Borst (2013) has been revisited. Following the difficulties that were encountered in extending this

approach to arbitrary crack paths and unstructured meshes, a simple patch test was devised, in which boundary conditions were applied to a square specimen, such that a uniform, uniaxial stress state should be obtained. For a structured mesh this indeed appeared the case, but stress oscillations were found when displacing the nodes in a patch of four elements. This unfortuntaly renders the current state of the cohesive phase-field approach to fracture not applicable to arbitrary loading configurations and discretisations.

References

Ambrosio, L., Tortorelli, V.M., 1990. Approximation of functional depending on jumps by elliptic functional via Γ-convergence. Communications on Pure and Applied Mathematics 43, 999–1036.

Amor, H., Marigo, J.J., Maurini, C., 2009. Regularized formulation of the variational brittle fracture with unilateral contact: Numerical experiments. Journal of the Mechanics and Physics of Solids 57, 1209–1229.

Bažant, Z.P., Oh, B., 1983. Crack band theory for fracture of concrete. RILEM Materials and Structures 16, 155–177.

Bellettini, G., Coscia, A., 1994. Discrete approximation of a free discontinuity problem. Discrete Functional Analysis and Optimization 15, 201–224.

Belytschko, T., Black, T., 1999. Elastic crack growth in finite elements with minimal remeshing. International Journal for Numerical Methods in Engineering 45, 601–620.

Borden, M.J., 2012. Isogeometric Analysis of Phase-Field Models for Dynamic Brittle and Ductile Fracture. PhD Thesis, The University of Texas at Austin.

Borden, M.J., Hughes, T.J.R., Landis, C.M., Verhoosel, C.V., 2014. A higher-order phase-field model for brittle fracture: Formulation and analysis within the isogeometric analysis framework. Computer Methods in Applied Mechanics and Engineering 273, 100–118.

Borden, M.J., Verhoosel, C.V., Scott, M.A., Hughes, T.J.R., Landis, C.M., 2012. A phase-field description of dynamic brittle fracture. Computer Methods in Applied Mechanics and Engineering 217-220, 77–95.

de Borst, R., Mühlhaus, H.B., 1992. Gradient-dependent plasticity: Formulation and algorithmic aspects. International Journal for Numerical Methods in Engineering 35, 521–539.

de Borst, R., Remmers, J.J.C., Needleman, A., Abellan, M.A., 2004. Discrete vs smeared crack models for concrete fracture: bridging the gap. International Journal for Numerical and Analytical Methods in Geomechanics 28, 583–607.

Bourdin, B., 2007. Numerical implementation of the variational formulation for quasi-brittle fracture. Interfaces and Free Boundaries 9, 411–430.

Bourdin, B., Francfort, G.A., Marigo, J.J., 2000. Numerical experiments in revisited brittle fracture. Journal of the Mechanics and Physics of Solids 48, 797–826.

Bourdin, B., Francfort, G.A., Marigo, J.J., 2008. The variational approach to fracture. Journal of Elasticity 91, 5–148.

Braides, A., 1998. Approximation of free-discontinuity problems. Springer Lecture Notes in Mathematics 1694.

Camacho, G.T., Ortiz, M.A., 1996. Computational modelling of impact damage in brittle materials. International Journal of Solids and Structures 33, 2899–2938.

Chambolle, A., 2004. An approximation result for special functions with bounded deformation. Journal de Mathématiques Pures et Appliquées 83, 929–954.

Francfort, G.A., Marigo, J.J., 1998. Revisiting brittle fracture as an energy minimization problem. Journal of the Mechanics and Physics of Solids 46, 1319–1342.

Hosseini, S., Remmers, J.J.C., Verhoosel, C.V., de Borst, R., 2014. An isogeometric continuum shell element for non-linear analysis. Computer Methods in Applied Mechanics and Engineering 271, 1–22.

Jiràsek, M., Bažant, Z.P., 2001. Inelastic Analysis of Structures. Wiley, Chichester.

Kuhn, C., Müller, R., 2010. A continuum phase field model for fracture. Engineering Fracture Mechanics 77, 3625–3634.

May, S., Vignollet, J., de Borst, R., 2014. An energy-based arc-length method. Engineering Computations, in preparation .

Miehe, C., Hofacker, M., Welschinger, F., 2010a. A phase field model for rate-independent crack propagation: Robust algorithmic implementation based on operator splits. Computer Methods in Applied Mechanics and Engineering 199, 2765–2778.

Miehe, C., Welschinger, F., Hofacker, M., 2010b. Thermodynamically consistent phase-field models of fracture: Variational principles and multi-field fe implementations. International Journal for Numerical Methods in Engineering 83, 1273–1311.

Moës, N., Belytschko, T., 2002. Extended finite element method for cohesive crack growth. Engineering Fracture Mechanics 69, 813–833.

Moës, N., Dolbow, J., Belytschko, T., 1999. A finite element method for crack growth without remeshing. International Journal for Numerical Methods in Engineering 46, 131–150.

Mumford, D., Shah, J., 1989. Optimal approximations by piecewise smooth functions and associated variational problems. Communications on Pure and Applied Mathematics 42, 577–685.

Ngo, D., Scordelis, A.C., 1967. Finite element analysis of reinforced concrete beams. Journal of the American Concrete Institute 64, 152–163.

Peerlings, R.H.J., de Borst, R., Brekelmans, W.A.M., de Vree, H.P.J., 1996. Gradient-enhanced damage for quasi-brittle materials. International Journal for Numerical Methods in Engineering 39, 3391–3403.

Pham, K., Amor, H., Marigo, J.J., Maurini, C., 2011. Gradient damage models and their use to approximate brittle fracture. International Journal of Damage Mechanics 20, 681–652.

Pham, K., Marigo, J.J., 2013. From the onset of damage until the rupture: construction of the responses with damage localization for a general class of gradient damage models. Continuum Mechanics and Thermodynamics 25, 147–171.

Piero, G.D., Lancioni, G., March, R., 2007. A variational model for fracture mechanics: numerical experiments. Journal of the Mechanics and Physics of Solids 55, 2513–2537.

Pijaudier-Cabot, G., Bažant, Z.P., 1987. Nonlocal damage theory. ASCE Journal of Engineering Mechanics 113, 1512–1533.

Rashid, Y.R., 1968. Analysis of reinforced concrete pressure vessels. Nuclear Engineering and Design 7, 334–344.

Remmers, J.J.C., de Borst, R., Needleman, A., 2003. A cohesive segments method for the simulation of crack growth. Computational Mechanics 31, 69–77.

Verhoosel, C.V., de Borst, R., 2013. A phase-field model for cohesive fracture. International Journal for Numerical Methods in Engineering 96, 43–62.

Verhoosel, C.V., Remmers, J.J.C., Gutiérrez, M.A., 2009. A dissipation-based arc-length method for robust simulation of brittle and ductile failure. International Journal for Numerical Methods in Engineering 77, 1290–1321.

Verhoosel, C.V., Scott, M.A., de Borst, R., Hughes, T.J.R., 2011. An isogeometric approach to cohesive zone modeling. International Journal for Numerical Methods in Engineering 87, 336–360.

Vignollet, J., May, S., de Borst, R., Verhoosel, C.V., 2014. Phase-field models for brittle and cohesive fracture. Meccanica , 1–15.

Wawrzynek, P.A., Ingraffea, A.R., 1987. Interactive finite element analysis of fracture processes: an integrated approach. Theoretical and Applied Fracture Mechanics 8, 137–150.

Wells, G.N., Sluys, L.J., 2001. A new method for modelling cohesive cracks using finite elements. International Journal for Numerical Methods in Engineering 50, 2667–2682.